



Cite this: *J. Mater. Chem. A*, 2018, **6**, 21320Received 27th August 2018
Accepted 8th October 2018

DOI: 10.1039/c8ta08296k

rsc.li/materials-a

Sequential deposition route to efficient Sb₂S₃ solar cells†

Lijian Zhang,^a Chunyan Wu,^a Weifeng Liu,^a Shangfeng Yang,^a ^a Mingtai Wang,^b Tao Chen ^{*a} and Changfei Zhu^{*a}

We report a facile two-step sequential deposition method to prepare Sb₂S₃ thin films, where antimony acetate and thiourea are utilized as antimony and sulfur sources, respectively. The sequential deposition of two precursor materials followed by swift annealing at mild temperature leads to high-quality Sb₂S₃ films. The detailed reaction mechanism is revealed on the basis of structural and compositional analyses. By optimizing the concentration of thiourea and annealing temperature, uniform and flat Sb₂S₃ thin films are obtained with either sulfur-deficiency or sulfur richness. Finally, a planar heterojunction solar cell based on the as-prepared Sb₂S₃ film delivers a high power conversion efficiency of 5.69%, which is a top value for planar heterojunction Sb₂S₃ solar cells fabricated by a solution approach. This research provides a convenient and low-cost approach for the deposition of Sb₂S₃ films for efficient solar cell applications.

1. Introduction

The imperative requirement for high-efficiency, low-cost and environment friendly photovoltaics propels researchers in one way or another to explore new light absorbing materials for device construction.¹ In recent years, antimony sulfide (Sb₂S₃) has attracted more and more attention as a light harvesting material in solar cell research. It possesses attractive physical properties such as suitable band gap (~1.7 eV), high absorption coefficient (~10⁵ cm⁻¹ at 450 nm), air/moisture-stability and relative non-toxicity and earth-abundance of constituent elements.^{2–5} Notably, the band gap allows the application of Sb₂S₃ as a light absorbing material in either single junction solar cells or top cells in a tandem solar device coupled with narrow band gap silicon, Cu(In,Ga)Se₂ or perovskite solar cells.⁶ Intensive efforts have been exerted to improve the performance of Sb₂S₃ solar cells ranging from material synthesis to surface/defect engineering to device structure design.^{3,7–10} As one of the key components in solar devices, the quality of the absorbing layer plays a vital role in the photovoltaic performance of devices. Chemical bath deposition (CBD) was initially applied to synthesize Sb₂S₃ for solar cell applications and a PCE of 3.37% was achieved.¹¹ Afterwards, CBD was the widely used method for

the synthesis of Sb₂S₃ thin films.^{3,7,11,12} Indeed, the CBD approach is convenient and cost effective. Nevertheless, the formation of Sb₂S₃ is unavoidably accompanied by the production of antimony oxide, hydroxide or sulfate, resulting in deep traps in the gap state of Sb₂S₃ films.^{2,3,13} Post treatment is thus required to further improve the PCE. For instance, thioacetamide treatment has led to the highest reported PCE of 7.5% in mesoporous Sb₂S₃-sensitized solar cells.³ It is also noted that the CBD method usually requires a long time (several hours) for obtaining Sb₂S₃ films with appropriate thickness. Zheng *et al.* developed a fast solid-gas reaction for an antimony sulfide absorber and yielded a PCE of 6.27%.² By using a TiO₂ nanorod array as the electron extraction material, a spin-coating based method has delivered 6.8% efficiency in Sb₂S₃ solar cells.¹⁴ It is worth noting that all of the above investigations are based on sensitized device structures. In fact, the high efficiencies are exclusively achieved in a sensitized device configuration.

With regard to practical applications, a planar heterojunction solar cell is advantageous in terms of convenient and continuous production. However, the PCE of planar heterojunction solar cells based on CBD-derived Sb₂S₃ films is generally below 5%.^{15–18} Apart from the CBD method, the atomic layer deposition (ALD) technique with precise thickness control was used to deposit a high purity Sb₂S₃ film on a planar TiO₂ film with a PCE of 5.77%.¹³ However, the slow growth rate of 100–300 nm h⁻¹ as well as its requirements of ultrahigh vacuum conditions and complex and expensive instrumentation limits its large-scale application at low cost.^{4,19} Our group has developed a series of solution approaches for the synthesis of Sb₂S₃ as well as Sb₂(S,Se)₃ films for planar heterojunction solar cells, obtaining ~5% efficiency in Sb₂S₃ solar cells and 5.8% in

^aCAS Key Laboratory of Materials for Energy Conversion, Department of Materials Science and Engineering, University of Science and Technology of China, No. 96 Jinzhai Road, Hefei, Anhui 230026, P. R. China. E-mail: tchenmse@ustc.edu.cn; cfzhu@ustc.edu.cn

^bInstitute of Applied Technology, Hefei Institutes of Physical Science, Chinese Academy of Sciences, Hefei, Anhui 230031, P. R. China

† Electronic supplementary information (ESI) available: Additional XRD and Raman spectra of Sb₂S₃ along with the statistical distribution of V_{OC}, J_{SC}, and FF. See DOI: 10.1039/c8ta08296k

$\text{Sb}_2(\text{S,Se})_3$ solar cells.^{5,10,20,21} Thermal evaporation deposition was also applied in the deposition of Sb_2S_3 films, while the efficiency (around 4%) is considerably lower than that of the solution processed Sb_2S_3 films.^{9,22,23} Therefore, it is highly desirable to develop effective approaches for fabricating high efficiency planar heterojunction Sb_2S_3 thin film solar cells.

In the present work, a convenient two-step sequential deposition approach for rapid deposition of a Sb_2S_3 thin film on a compact TiO_2 (c- TiO_2) film is introduced. In this approach, the antimony acetate ($\text{Sb}(\text{Ac})_3$) layer was first spin-coated on the c- TiO_2 film from the dimethyl sulfoxide (DMSO) solution. Consequently, the thiourea (TU) solution was spin-coated onto the surface. Upon annealing at mild temperature, the reaction between $\text{Sb}(\text{Ac})_3$ and TU leads to the formation of the Sb_2S_3 film. Strikingly, this transformation can occur in less than 2 minutes. A planar heterojunction solar cell based on this Sb_2S_3 thin film delivers an optimized PCE of 5.69%. It is worth noting that an additional post-annealing process, such as sulfurization or selenization, is not necessary in our process.

2. Results and discussion

Fig. 1 displays a schematic illustration of the synthesis of the Sb_2S_3 film on the c- TiO_2 /fluorine doped tin oxide (FTO)

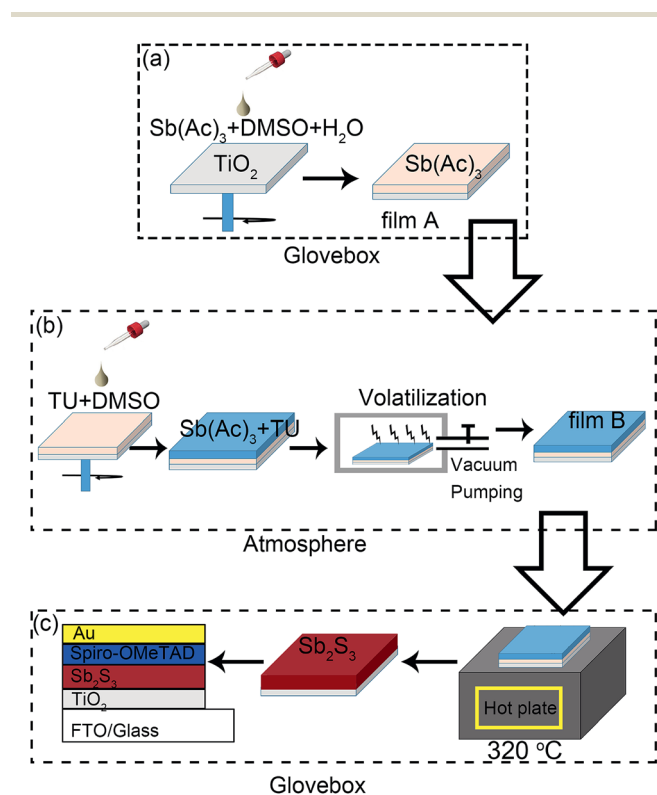


Fig. 1 Schematic illustration of the film deposition and device fabrication. (a) Spin-coating $\text{Sb}(\text{Ac})_3$ in DMSO solution for the fabrication of the $\text{Sb}(\text{Ac})_3$ film (film A). (b) Deposition of thiourea (TU) on the surface of film A, followed by dissociating the organic molecule using a vacuum pump (film B). (c) Annealing of film B at an elevated temperature for the formation of the crystallized Sb_2S_3 film and device assembly.

substrate by the sequential deposition method. For deposition of the Sb_2S_3 thin film, 0.5 g $\text{Sb}(\text{Ac})_3$ was first dissolved in a DMSO and H_2O mixed solvent with a volume ratio of 800 : 30. It was then spin-coated on the FTO glass substrate pre-coated with a compact TiO_2 film (details are provided in the Experimental section). This $\text{Sb}(\text{Ac})_3$ film is denoted as film A. Subsequently, a series of concentrations of TU in DMSO (4, 6 and 8 mol L^{-1}) were spin-coated onto film A in air for the following device optimizations. To dissociate the solvent, the film was placed in a vacuum chamber for 2 min (denoted as film B). Finally, the film was transferred to a glove box and heated at elevated temperature on a hotplate to promote the reaction between $\text{Sb}(\text{Ac})_3$ and TU.

Upon thermal annealing, TU would be decomposed to generate H_2S .^{24,25} The reaction between H_2S and $\text{Sb}(\text{Ac})_3$ leads to the formation of Sb_2S_3 . In order to study how the pyrolysis temperature of TU influences the Sb_2S_3 transformation, the crystal structure of film B obtained by deposition of 6 M TU on the $\text{Sb}(\text{Ac})_3$ layer with further annealing at $150\text{ }^\circ\text{C}$, $200\text{ }^\circ\text{C}$, $250\text{ }^\circ\text{C}$ and $320\text{ }^\circ\text{C}$ for 2 min was characterized by X-ray diffraction (XRD) (Fig. 2a). As a control experiment, film A prepared by spin-coating $\text{Sb}(\text{Ac})_3$ on the FTO/c- TiO_2 substrate did not display any XRD peak except those from FTO (black line of Fig. 2a). After the deposition of 6 M TU and treatment at temperatures from $150\text{ }^\circ\text{C}$ to $250\text{ }^\circ\text{C}$, no diffraction peaks were found apart from FTO, while the color of the film changed from transparent to light yellow and then dark yellow (insets of Fig. 2a). The color change implies that H_2S is gradually generated from the thermal decomposition of TU and reacts with film A to form the amorphous Sb_2S_3 layer as characterized by Raman scattering (*vide infra*). As the temperature raised to $320\text{ }^\circ\text{C}$, a series of diffraction peaks at 15.64° , 17.52° , 22.27° , 24.88° , 29.24° , 32.35° , and 35.32° appeared, which exactly matched the orthorhombic Sb_2S_3 structure (JCPDS No. 42-1393).³ The detailed index is provided in Fig S1.† Notably, there are no impurity peaks observed, indicating that the phase transformation towards Sb_2S_3 is complete.

Although XRD characterization manifests the formation and crystallization at $320\text{ }^\circ\text{C}$, this does not mean that Sb_2S_3 did not form at low temperatures. The color changes as mentioned above would be an indication of the formation of Sb_2S_3 in the amorphous state. To establish a complete picture regarding this reaction, we characterize the samples annealed at $150\text{ }^\circ\text{C}$, $200\text{ }^\circ\text{C}$, $250\text{ }^\circ\text{C}$ and $320\text{ }^\circ\text{C}$ for 2 min by Raman scattering (Fig. 2b). For film A (*i.e.* $\text{Sb}(\text{Ac})_3$), only one peak at 144 cm^{-1} is found. When TU was deposited on it and annealed at 150, 200 and $250\text{ }^\circ\text{C}$, in addition to the Raman scattering from $\text{Sb}(\text{Ac})_3$ at 144 cm^{-1} , a broad peak at 281 cm^{-1} is observed, which is assigned to amorphous Sb_2S_3 .^{26,27} This result indicates that the formation of Sb_2S_3 occurs at a relatively low temperature. The high reactivity of generated H_2S is responsible for this reaction. Furthermore, when the temperature reaches $320\text{ }^\circ\text{C}$, the peak at 144 cm^{-1} disappeared and typical Raman scattering at 279.8 and 299 cm^{-1} (C_{3v} symmetry of the Sb_2S_3 pyramidal unit), along with 124, 151, 185, 236, 279, and 299 cm^{-1} , are observed, corresponding to the Sb_2S_3 stibnite phase.^{28–30} This characterization again indicates the complete phase transformation from the precursor film to Sb_2S_3 .

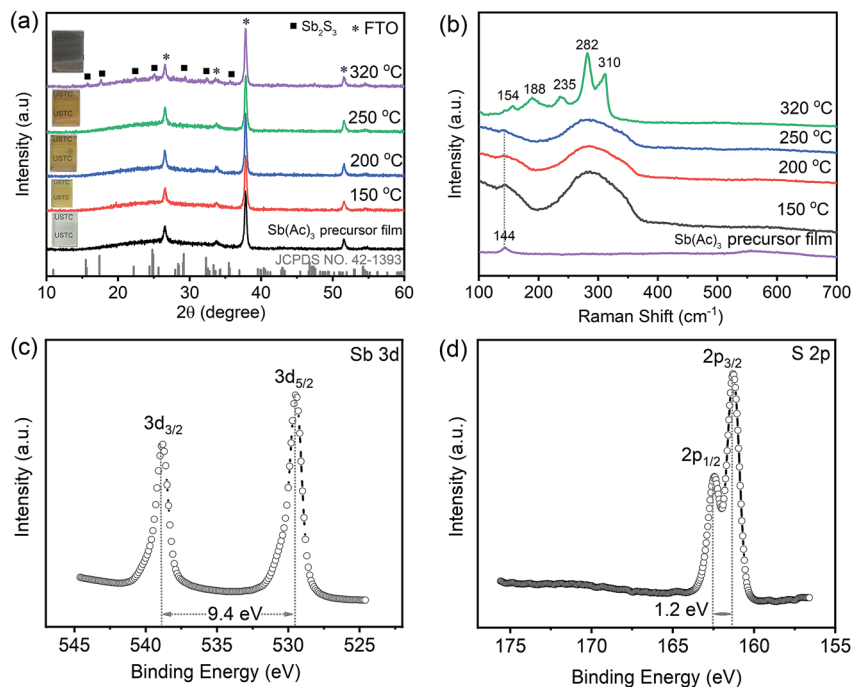


Fig. 2 Structure and composition characterization. (a) XRD patterns and (b) Raman scattering spectra of Sb_2S_3 thin films prepared from 6 M TU deposited on the $\text{Sb}(\text{Ac})_3$ film followed by annealing at 150 °C, 200 °C, 250 °C and 320 °C for 2 min, respectively; XPS spectra of (c) Sb 3d and (d) S 2p obtained from the 6 M TU deposited on the Sb-Salt film and annealed at 320 °C for 2 min.

In order to verify the valence states of the Sb_2S_3 film grown at 320 °C, X-ray photoelectron spectroscopy (XPS) was conducted. The core spectra of Sb 3d and S 2p are shown in Fig. 2c and d, respectively. Two typical peaks at 529.5 eV and 538.9 eV associated with Sb $3d_{5/2}$ and Sb $3d_{3/2}$ binding energies are indexed to the oxidation state of Sb^{3+} in Sb_2S_3 .^{31,32} The peaks located at 162.3 and 161.1 eV are assigned to $2p_{3/2}$ and $2p_{1/2}$ of the S^{2-} oxidation state of Sb_2S_3 .^{3,31–33} The separation of the Sb 3d doublet and the S 2p doublet are 9.4 and 1.2 eV, respectively. This XPS result reaffirms the formation of Sb_2S_3 from the reaction between $\text{Sb}(\text{Ac})_3$ and TU at 320 °C through the sequential deposition method.

The uniformity of the surface morphology of the absorber film critically influences the device performance. In this case, we study the surface morphologies of the as-synthesized film associated with different TU concentrations. As a control characterization, the scanning electron microscope (SEM) image of film A shows mesoporous characteristics (Fig. 3a and b); this morphology would increase the contact area between $\text{Sb}(\text{Ac})_3$ and TU and promote the complete transformation towards Sb_2S_3 . The morphologies of Sb_2S_3 treated at 320 °C with the TU concentration of 4 M, 6 M, and 8 M are shown in Fig. 3c–h. The corresponding XRD and Raman spectra are also displayed in Fig. S2,[†] indicating the pure Sb_2S_3 phase. At the TU concentration of 4 M, the generated Sb_2S_3 film displays a compact surface morphology with a few pin holes (Fig. 3c and d). When the concentration increases to 6 M, pin holes are considerably reduced with more compact film morphology (Fig. 3e and f). With the TU concentration of 8 M, the uniformity is essentially decreased at low magnification (Fig. 3g), although the high

magnification image exhibits compact features in selected areas (Fig. 3h). On further increasing the TU concentration (>8 M), the Sb_2S_3 film was found to decompose (data not shown). Presumably, when a large excess concentration of TU was spin-coated on film A and then treated at 320 °C, a large amount of by-products from TU decomposition including NH_4SCN , NH_3 , and HNCS would be formed.^{25,34} These excess by-products especially NH_3 may destroy the Sb_2S_3 thin film since Sb_2S_3 is soluble in alkaline solution.³⁵ Therefore, a suitable concentration of TU should be adopted to obtain a high quality Sb_2S_3 film.

Furthermore, energy-dispersive X-ray spectroscopy (EDS) was carried out to establish the correlation between TU concentration and the atomic ratio of S/Sb in the as-synthesized Sb_2S_3 films. As shown in Fig. 3i, when the TU concentration is 4 M, S/Sb is 1.22, which represents the sulfur deficit phase and may result in deep traps.^{6,9} With the TU concentration increasing to 6 M and 8 M, the S/Sb ratio increases to 1.77 to 1.85, implying that sulfur rich phases are formed. This tunability allows probing defect dependent device performance.

The UV-vis absorption spectra of Sb_2S_3 prepared from 4 M, 6 M and 8 M TU are shown in Fig. 3j. The onset absorption of the three films locates at 700 nm. The absorption intensity of Sb_2S_3 obtained from 4 M TU is lower than that obtained from 6 M and 8 M TU. This is mainly due to less H_2S generated from 4 M TU that is unable to induce complete transformation from $\text{Sb}(\text{Ac})_3$ to Sb_2S_3 . The band gaps of those three samples are estimated to be around 1.78 eV by extrapolating the linear region of a plot of the squared absorbance versus the photon energy according to the absorption spectra (inset of Fig. 3j).

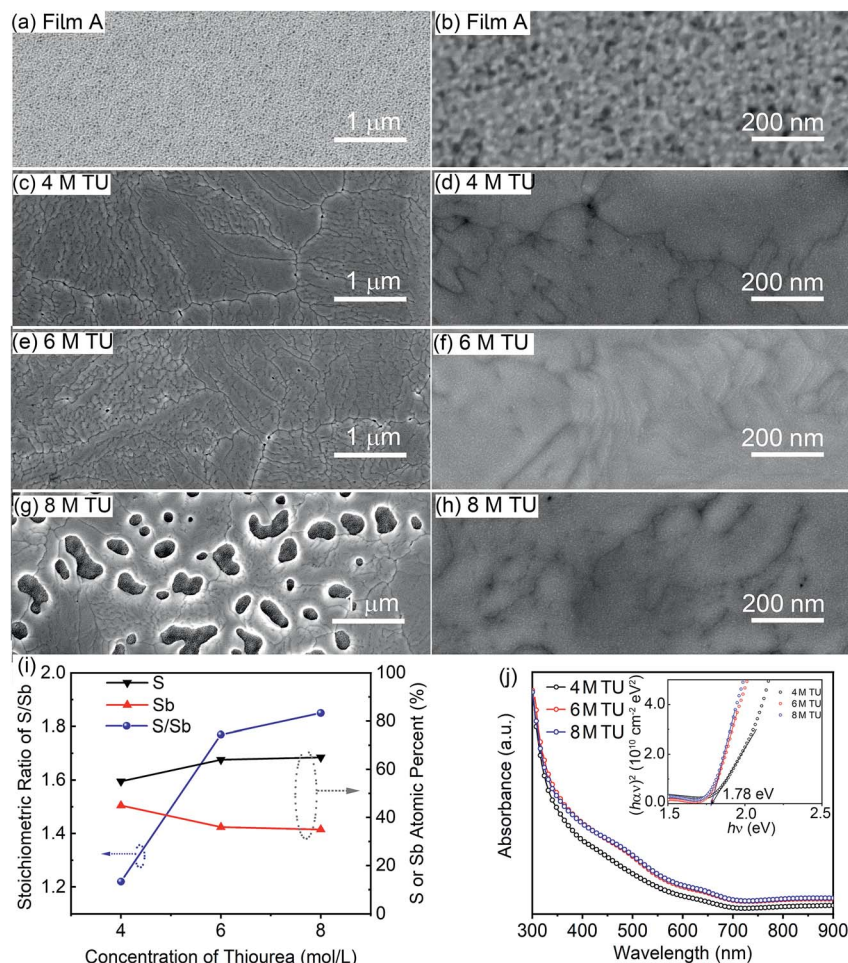


Fig. 3 Surface morphology characterization, composition analysis and light absorption characterization. (a) Low and (b) high magnification surface SEM images of the $\text{Sb}(\text{Ac})_3$ film, (c, e, g) low and (d, f, h) high magnification surface SEM images of the $\text{Sb}(\text{Ac})_3$ film reacted with spin-coated TU with concentrations of 4 M, 6 M and 8 M TU, respectively, followed by annealing at 320°C for 2 min. (i) Atomic ratio of S/Sb and (j) UV-vis absorption spectra of Sb_2S_3 films prepared from 4 M, 6 M, and 8 M TU with annealing at 320°C for 2 min, respectively, the inset in (j) showing the corresponding Tauc plots.

Sb_2S_3 solar cells were fabricated by using c-TiO_2 and 2,2',7,7'-tetrakis(*N,N*-di-*p*-methoxyphenyl amine)-spirobifluorene (Spiro-OMeTAD) as electron and hole transporting materials, respectively. The device structure is depicted in Fig. 1, described as FTO/ c-TiO_2 / Sb_2S_3 /Spiro-OMeTAD/Au. The thickness of the TiO_2 compact layer and the optimal thickness of the Sb_2S_3 film, Spiro-OMeTAD and Au are measured to be 35, 62, 65, 30 nm as shown in Fig. 4a. The current density–voltage (J – V) behavior was measured under 1 Sun (AM 1.5G) illumination (Fig. 4b). The detailed photovoltaic parameters are summarized in Table 1. When 4 M TU was used, the device delivers a PCE of 2.77% with a short-circuit current density (J_{SC}) of 9.31 mA cm^{-2} , an open-circuit voltage (V_{OC}) of 0.65 V and a fill factor (FF) of 45.73%. Strikingly, once the concentration of TU is increased to 6 M, the PCE soared to 5.69%, with J_{SC} , V_{OC} and FF of 14.34 mA cm^{-2} , 0.66 V and 60.43%. Both J_{SC} and FF are considerably enhanced. The efficiency enhancement should be associated with the Sb/S ratio in the Sb_2S_3 films. At the TU concentration of 4 M, the S/Sb ratio is 1.22 (Fig. 3i). This sulfur deficiency is prone to inducing sulfide radical species in Sb_2S_3 , which act as hole trap sites and causes the

slow extraction of holes compared to electrons, finally leading to increased recombination at the $\text{TiO}_2/\text{Sb}_2\text{S}_3$ interface so that the device performance deteriorates.^{3,4,36} While the use of 6 M TU can generate more abundant of H_2S which can react with film A to form S-rich Sb_2S_3 phase. This S-rich Sb_2S_3 phase had lower the defect concentration which can boosted photovoltaic energy conversion efficiency. However, when the TU concentration increases to 8 M, the PCE decreases to 4.27%. In this case, although the sulfur richness is a positive effect, the formation of large holes (Fig. 3g) would compromise this favorable effect. This kind of pin hole induces direct contact between the hole transporting layer and electron transporting layer, which in turn results in increased recombination probability. The statistical distribution of V_{OC} , J_{SC} , FF (Fig. S3†) and PCE of 59 devices fabricated under optimized conditions (with a TU of 6 M) is shown in Fig. 4c. The PCE is in the range of 4.01%–5.69% and the average PCE is 5.01% (Table 1). Furthermore, there are 35 devices showing PCEs exceeding 5%, indicating good reproducibility of this fabrication method. At the best TU concentrations (6 M), we also optimized the film thickness (from 60 to 120 nm) for device performance

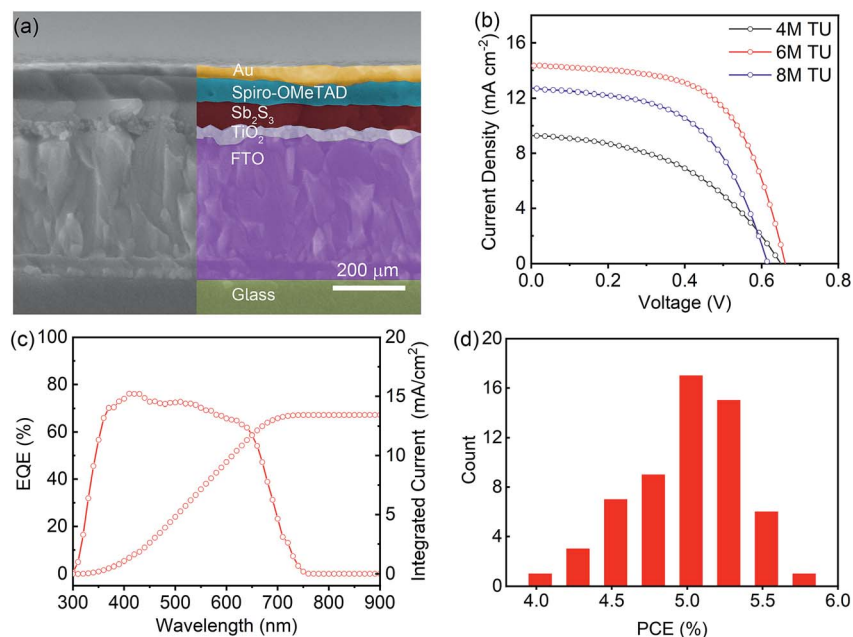


Fig. 4 Device performance characterization. (a) SEM image of the cross section of the fabricated Sb_2S_3 solar cell. (b) Current density–voltage curves of solar cells with Sb_2S_3 thin films prepared from 4 M, 6 M, and 8 M TU with post annealing at 320°C for 2 min. (c) EQE and integrated photocurrent spectra of the best device with the Sb_2S_3 film fabricated by the reaction between the $\text{Sb}(\text{Ac})_3$ film and TU under 6 M. (d) Histogram of device efficiencies obtained from 59 individually fabricated devices under optimized conditions.

Table 1 Photovoltaic performance (V_{OC} , J_{SC} , FF and PCE) of the solar devices with Sb_2S_3 films fabricated using TU concentrations of 4 M, 6 M, and 8 M TU and annealing at 320°C for 2 min

	4 M TU	6 M TU ^a	8 M TU
PCE (%)	2.77	5.69 (5.01 ± 0.36)	4.27
V_{OC} (V)	0.65	0.66 (0.63 ± 0.02)	0.61
FF (%)	45.73	60.43 (58.10 ± 2.03)	54.74
J_{SC} (mA cm^{-2})	9.31	14.34 (13.63 ± 0.70)	12.71

^a The V_{OC} , J_{SC} , FF and PCE in the brackets are average device parameters.

investigations (Table S1 and Fig. S4†). It turns out that the thickness of around 60 nm generates the highest PCE. In this case, we propose that if the thickness of the $\text{Sb}(\text{AC})_3$ film is increased, TU may not penetrate into the bottom of the solid $\text{Sb}(\text{AC})_3$ film, resulting in an incomplete reaction between $\text{Sb}(\text{AC})_3$ and TU. The residue $\text{Sb}(\text{AC})_3$ generates a negative effect on the device performance.

The external quantum efficiency (EQE) spectrum of the best device is shown in Fig. 4c. The photocurrent generation of the best-performing device exceeds 70% in longer wavelengths and 80% in short wavelengths, indicating the effectiveness of using this sequential deposition method for the fabrication of Sb_2S_3 solar cells. The J_{SC} integrated from the EQE data is 13.44 mA cm^{-2} , which is quite close to the J_{SC} obtained from the J - V measurement (14.34 mA cm^{-2}).

3. Conclusions

In summary, for the first time we have demonstrated a sequential deposition approach for the fabrication of Sb_2S_3

thin films by using antimony acetate and thiourea as reaction precursors. The transformation towards the Sb_2S_3 film only requires 2 min at a mild temperature. The mechanistic investigation shows that amorphous Sb_2S_3 can be easily formed at a very low temperature (150°C) through the reaction between $\text{Sb}(\text{Ac})_3$ and H_2S generated from the pyrolysis of thiourea. The amorphous Sb_2S_3 crystallizes when the annealing temperature increases to 320°C . We found that the concentration of TU is crucial for improving the device performance. The low concentration of TU would form a sulfur deficit vacancy resulting in deep traps in the Sb_2S_3 films. While the higher concentration of TU brings forth large pin holes in the Sb_2S_3 films. Since the film is very thin, the Sb_2S_3 thin film obtained by this method can be semi-transparent (Fig. S5†), offering potential for the fabrication of transparent solar cells. Finally, this approach is effective and delivers a device efficiency of 5.69%, which is among the top values for planar heterojunction Sb_2S_3 solar cells fabricated by a solution approach.

4. Experiment

4.1. Materials

Antimony(III) acetate ($\text{C}_6\text{H}_9\text{O}_6\text{Sb}$, 97%) was purchased from Alfa. Titanium isopropoxide (TIPT), lithium bis(trifluoromethylsulfonyl)imide (Li-TFSI), 4-*tert*-butylpyridine (*t*BP), ultra-dry dimethyl sulfoxide (DMSO) and chlorobenzene were purchased from J&K. Thiourea (TU, AR) was purchased from Sinopharm, China. Spiro-OMeTAD (99.8%) was purchased from Youxuan Tech., Ltd. All chemicals were used as received without further purification.

4.2. Synthesis of the precursor solution

The preparation of the antimony(III) acetate precursor solution was conducted by mixing 0.5 g antimony(III) acetate and 0.8 mL DMSO and H₂O mixed solvent with a volume ratio of 800/30 in a 5 mL vial in a glove box. The addition of H₂O would increase the solution viscosity on the one hand and thus promote the film formation. Then, the mixed solution was stirred at room temperature for 30 min. The TU solution was prepared by mixing 4 mol, 6 mol and 8 mol TU and 1 mL DMSO in a 5 mL vial and stirred at 50 °C for 1 hour.

4.3. Synthesis of Sb₂S₃ film and device fabrication

To prepare antimony(III) acetate precursor thin films, the Sb(Ac)₃ precursor solution was spin-coated on the compact layer of TiO₂ (c-TiO₂) at a speed of 5000 rpm for 30 s in the glove box. Afterwards, TU solutions with different concentrations were spin-coated onto the pre-formed Sb(Ac)₃ precursor film at 3000 rpm for 30 s in air. After that, the film was transferred into a vacuum chamber for 2 min to evaporate the solvent out. Finally, the film was transferred into the glove box and put on a hotplate for annealing at different temperatures for 2 min to complete the phase transformation.

The solar cell device was fabricated with the structure of FTO/c-TiO₂/Sb₂S₃/Spiro-OMeTAD/Au. First, FTO-coated glass was cleaned using deionized water, isopropanol, acetone and anhydrous alcohol for 40 min in each solvent. Afterwards, c-TiO₂ was deposited on the pre-cleaned FTO-coated glass substrate by spin-coating a mixture solution of 140 μL of titanium isopropoxide, 2 mL of ethanol, and 26 μL of 2 mol mL⁻¹ hydrochloric acid (HCl, diluted by ethanol) at 3000 rpm for 30 s, followed by annealing at 550 °C for 30 min in air. The Sb₂S₃ film was fabricated on c-TiO₂ according to the above methods. The Spiro-OMeTAD solution was prepared by mixing 36.6 mg of spiro-OMeTAD, 14.5 μL of 4-*tert*-butylpyridine (*t*BP) and 9.5 μL of a 520 mg mL⁻¹ lithium bis(trifluoromethanesulfonyl)imide (Li-TFSI) together in 1 mL of chlorobenzene. After that, the Spiro-OMeTAD solution was spin-coated on the FTO/c-TiO₂/Sb₂S₃ substrate at a speed of 3000 rpm for 30 s and heated on a hotplate at 100 °C for 10 min in air. Finally, the Au electrode was deposited using a thermal evaporator under a pressure of 5.0 × 10⁻⁴ Pa. It is worth noting that the device without the hole transporting material did not exhibit any photovoltaic energy conversion. The active area of the device was defined as 0.12 cm⁻².

4.4. Characterization

The samples were characterized by powder X-ray diffraction (XRD) on a Bruker Advance D8 diffractometer equipped with Cu K α radiation ($\lambda = 1.5416 \text{ \AA}$). The optical characteristics of the films were measured with a UV-visible spectrophotometer (SOLID 3700). The Raman spectra of the solutions were obtained at room temperature using a LABRAM-HR Evolution system in the backscattering configuration with a 532 nm Ar laser with the power adjusted to 4 mW. The surface and cross sectional morphologies of the samples were examined by SEM

(SU8200). X-ray photoelectron spectroscopy (XPS) was conducted on a Thermo ESCALAB 250Xi system with an Al K α monochromatized source and a multi-detection analyzer under 10⁻⁸ Torr. Finally, the *J*-*V* curves were recorded using a Keithley 2400 apparatus using solar-simulated AM 1.5 sunlight (100 mW cm⁻²) with a standard xenon-lamp-based solar simulator (Oriel Sol 3A, Japan). The solar simulator illumination intensity was calibrated by using a monocrystalline silicon reference cell (Oriel P/N 91150 V, with a KG-5 visible color filter) calibrated by the National Renewable Energy Laboratory (NREL). The external quantum efficiency (EQE, Model SPIEQ200) was measured using a single source illumination system (halogen lamp) combined with a monochromator.

Conflicts of interest

There are no conflicts to declare.

Acknowledgements

This work was supported by the Fundamental Research Funds for the Central Universities under No. WK2060140023, WK2060140022, CX3430000001, WK2060140024, the Major/Innovative Program of Development Foundation of Hefei Center for Physical Science and Technology (2016FXZY003), and the Recruitment Program of Global Experts (National Natural Science Foundation of China (GG2060140085)).

Notes and references

- M. A. Green, Y. Hishikawa, E. D. Dunlop, D. H. Levi, J. Hohl-Ebinger and A. W. Ho-Baillie, *Prog. Photovoltaics*, 2018, **26**, 427–436.
- L. Zheng, K. Jiang, J. Huang, Y. Zhang, B. Bao, X. Zhou, H. Wang, B. Guan, L. M. Yang and Y. Song, *J. Mater. Chem. A*, 2017, **5**, 4791–4796.
- Y. C. Choi, D. U. Lee, J. H. Noh, E. K. Kim and S. I. Seok, *Adv. Funct. Mater.*, 2014, **24**, 3587–3592.
- Y. C. Choi and S. I. Seok, *Adv. Funct. Mater.*, 2015, **25**, 2892–2898.
- C. Wu, L. Zhang, H. Ding, H. Ju, X. Jin, X. Wang, C. Zhu and T. Chen, *Sol. Energy Mater. Sol. Cells*, 2018, **183**, 52–58.
- R. Kondrotas, C. Chen and J. Tang, *Joule*, 2018, **2**, 857–878.
- S. Ito, K. Tsujimoto, D.-C. Nguyen, K. Manabe and H. Nishino, *Int. J. Hydrogen Energy*, 2013, **38**, 16749–16754.
- T. Fukumoto, T. Moehl, Y. Niwa, M. K. Nazeeruddin, M. Grätzel and L. Etgar, *Adv. Energy Mater.*, 2013, **3**, 29–33.
- S. Yuan, H. Deng, X. Yang, C. Hu, J. Khan, W. Ye, J. Tang and H. Song, *ACS Photonics*, 2017, **4**, 2862–2870.
- L. Zhang, C. Jiang, C. Wu, H. Ju, G. Jiang, W. Liu, C. Zhu and T. Chen, *ACS Appl. Mater. Interfaces*, 2018, **10**, 27098–27105.
- Y. Itzhak, O. Niitsoo, M. Page and G. Hodes, *J. Phys. Chem. C*, 2009, **113**, 4254–4256.
- J. A. Chang, J. H. Rhee, S. H. Im, Y. H. Lee, H. J. Kim, S. I. Seok, M. K. Nazeeruddin and M. Grätzel, *Nano Lett.*, 2010, **10**, 2609–2612.

- 13 D. H. Kim, S. J. Lee, M. S. Park, J. K. Kang, J. H. Heo, S. H. Im and S. J. Sung, *Nanoscale*, 2014, **6**, 14549–14554.
- 14 R. Tang, X. Wang, C. Jiang, G. Jiang, S. Yang, C. Zhu and T. Chen, *J. Mater. Chem. A*, 2018, **6**, 16322–16327.
- 15 H. Lei, G. Yang, Y. Guo, L. Xiong, P. Qin, X. Dai, X. Zheng, W. Ke, H. Tao, Z. Chen, B. Li and G. Fang, *Phys. Chem. Chem. Phys.*, 2016, **18**, 16436–16443.
- 16 X. Zhang, Z. Lan, S. Cao, J. Wang and Z. Chen, *Ionics*, 2014, **21**, 1781–1786.
- 17 Y. Osorio Mayon, T. P. White, R. Wang, Z. Yang and K. R. Catchpole, *Phys. Status Solidi A*, 2016, **213**, 108–113.
- 18 Y. Zhang, S. Li, R. Tang, X. Wang, C. Chen, W. Lian, C. Zhu and T. Chen, *Energy Technol.*, 2018, **6**, 1–7.
- 19 M. Leskela and M. Ritala, *Angew. Chem., Int. Ed.*, 2003, **42**, 5548–5554.
- 20 X. Wang, J. Li, W. Liu, S. Yang, C. Zhu and T. Chen, *Nanoscale*, 2017, **9**, 3386–3390.
- 21 S. Li, Y. Zhang, R. Tang, X. Wang, T. Zhang, G. Jiang, W. Liu, C. Zhu and T. Chen, *ChemSusChem*, 2018, **11**, 1–8.
- 22 S. Yuan, H. Deng, D. Dong, X. Yang, K. Qiao, C. Hu, H. Song, H. Song, Z. He and J. Tang, *Sol. Energy Mater. Sol. Cells*, 2016, **157**, 887–893.
- 23 X. Chen, Z. Li, H. Zhu, Y. Wang, B. Liang, J. Chen, Y. Xu and Y. Mai, *J. Mater. Chem. C*, 2017, **5**, 9421–9428.
- 24 V. Timchenko, A. Novozhilov and O. Slepysheva, *Russ. J. Gen. Chem.*, 2004, **74**, 1046–1050.
- 25 Z. D. Wang, M. Yoshida and B. George, *Comput. Theor. Chem.*, 2013, **1017**, 91–98.
- 26 F. Perales, G. Lifante, F. Agulló-Rueda and C. d. I. Heras, *J. Phys. D: Appl. Phys.*, 2007, **40**, 2440–2444.
- 27 C. Gao, M. Xu, B. K. Ng, L. Kang, L. Jiang, Y. Lai and F. Liu, *Mater. Lett.*, 2017, **195**, 186–189.
- 28 P. Makreski, G. Petruševski, S. Ugarković and G. Jovanovski, *Vib. Spectrosc.*, 2013, **68**, 177–182.
- 29 R. Boughalmi, A. Boukhachem, M. Kahlaoui, H. Maghraoui and M. Amlouk, *Mater. Sci. Semicond. Process.*, 2014, **26**, 593–602.
- 30 R. G. Sotelo Marquina, T. G. Sanchez, N. R. Mathews and X. Mathew, *Mater. Res. Bull.*, 2017, **90**, 285–294.
- 31 J. Ota and S. K. Srivastava, *Cryst. Growth Des.*, 2007, **7**, 343–347.
- 32 M. S. You, C.-S. Lim, D. H. Kwon, J. H. Heo, S. H. Im and K. J. Chae, *Org. Electron.*, 2015, **21**, 155–159.
- 33 R. G. Avilez Garcia, C. A. Meza Avendaño, M. Pal, F. Paraguay Delgado and N. R. Mathews, *Mater. Sci. Semicond. Process.*, 2016, **44**, 91–100.
- 34 S. Wang, Q. Gao and J. Wang, *J. Phys. Chem. B*, 2005, **109**, 17281–17289.
- 35 E. Sminčáková, *JOM*, 2009, **61**, 32–35.
- 36 J. A. Christians and P. V. Kamat, *ACS Nano*, 2013, **7**, 7967–7974.